Effect of Ion Irradiation on Surface Microstructure and Nano-Hardness of SA508-IV Reactor Pressure Vessel Steel

Xue Bai, Yun Han, Peter K. Liaw, and Lijun Wei

A new type SA508-IV reactor pressure vessel steel was irradiated at 290 °C to 3 and 30 displacement per atom (dpa) with 3.5 MeV Fe^{2+} ions. The focused ion beam was used to cut the samples for the field emission transmission electron microscope (FE-TEM) after irradiation. The microstructure analysis under the scanning transmission electron microscope (STEM) mode of FE-TEM revealed that the heavy ion irradiation produced a large number of matrix defects and Cu-rich clusters. The high dosage of irradiation would also force Mo atoms to relocate to form Cr/Mn/Mo-rich precipitates. Dislocation loops were especially formed in samples irradiated by 30 dpa, which are one of the principal evolving defects in irradiated materials. The nanoindentation test results showed that the nano-hardness increases with the increase of irradiation doses. The semi-plateau stage in 3 dpa irradiation (I3 sample) curve of nano-hardness versus indentation depth corresponds to the saturation of Cu-rich clusters; while the plateau stage in the I30 sample curve should be attributed to the loop coalescence.

1. Introduction

SA508-IV steel is a new type of reactor pressure vessel (RPV) steel, with a high content of nickel. It has been proved that this new RPV steel possesses relatively higher yield strength and low ductile-brittle transition temperature (Ref 1) than other steels, as well as improved fracture toughness because of the addition of 3 wt.% nickel (Ref 2, 3). Ni has been reported to improve low-temperature cleavage toughness by decreasing the energy barrier of kink formation (Ref 4, 5). However, there is still rather little knowledge about the properties of this steel, in particular its radiation resistance. In order to improve and design materials with better radiation resistance, it is essential to understand the microstructural features enhanced or induced by neutron irradiation. However, neutron irradiation experiments are expensive and radioactive. Some scientists used electron beam treatment to improve the surface state of steel (Ref 6), but the energy of electron beam is too low to simulate the neutron irradiation under long-term service life. It has been proven that the displacement cascades induced by ion irradiation are similar to those induced by neutron irradiation (Ref 7-9). Therefore, heavy ion irradiation is employed to produce irradiation damage for rapid simulation of the microstructural degradation and mechanical property deterioration of materials under neutron radiation (Ref 10, 11). Many point defects sites can be generated by ion bombardment through displacement cascades (Ref 12, 13).

Many scientists have focused on the irradiation-induced precipitates or clusters. In the low Cu-content RPV steel, Cu-rich atom clusters are the main irradiation-induced particles (Ref 14). It has been known that copper atoms in α-Fe tend to aggregate because of their low solubility (Ref 15). Odette et al. (Ref 16, 17) found that the formation of the precipitates or clusters has different stages, which means that they do not form at the same time. Cu-rich clusters (CRCs) usually form at the first stage; then the clusters which consist of Ni and Mn, without Cu form after that, thus the concept introduced is the so-called "late-blooming phases". Toyama et al. (Ref 18) used the advanced laser-assisted local electrode-type three dimensional-atom probe and demonstrated that the irradiation causes a series of atomic-distribution changes: Mn concentration within carbides increases, and the enhancement of Mn, Cr, and Mo concentration, as well as P segregation at the interface, are markedly intensified. On the other hand, matrix damage is also an important contributor to embrittlement. The cavities and dislocation loops are main matrix damages.

It is known that the microstructure evolution has different stages under low dose and high dose of irradiation. The nucleation and growth processes for the clusters or precipitates during ion irradiation are complex. Clarifying the irradiation response of the precipitates requires detailed characterization of nanoscale precipitates, including size, morphology, and composition before and after irradiation. The purpose of this work is to fully understand the irradiation-induced defects in SA508-IV RPV steel. The scanning electron microscope and transmission electron microscope are used to observe the microstructure evolution under ion irradiation. The continuous stiffness

Xue Bai, Shougang Research Institute of Technology, Beijing 100043, China; and Department of Materials Science and Engineering, The University of Tennessee, Knoxville, TN 37996; **Yun Han**, Shougang Research Institute of Technology, Beijing 100043, China; **Peter K. Liaw**, Department of Materials Science and Engineering, The University of Tennessee, Knoxville, TN 37996; and **Lijun Wei**, School of Materials Science and Engineering, Beihang University, Beijing 100191, China. Contact e-mail: 20051702bx@163.com.

measurement (CSM) method of nano-indentation is employed to obtain the profile of nano-hardness with the depth (Ref 19, 20). CSM curves could provide information about the clusters or precipitates.

2. Experimental Methods

2.1 Testing Materials and Irradiation Conditions

The material used in this study is the new generation SA508-IV RPV steel. The chemical compositions are listed in Table 1. This is a low-copper reactor pressure vessel steel, which contains 0.041 wt.% of Cu. The heat-treatment process of the as-received steel was held for 1.5 h at 920 °C, followed by water quenching to room temperature (RT), re-heating to 650 °C. for 30 h and then water cooling to RT. Heavy ion irradiation was conducted with 3.5 MeV Fe ions (Fe^{2+}) using the ion accelerator (under accelerating voltage of 1.7 MV) in Texas A&M University (USA), at 290 ± 5 °C. Before irradiation, the samples were cut into 3 mm × 3 mm ×1 mm, and one of the surfaces of 3 mm × 3 mm got grinded and polished, which would be the irradiation surface.

The stopping and ranges of ions in matters (SRIM) (Ref 21) calculations were used for the irradiation-damage calculation. The displacement damage and ion distribution versus depth are shown in Fig. 1. The displacement damage refers to vacancies, dislocations, and dislocation loops. It could be seen that the peak damage depth sits around 1000 nm below the ion irradiated surface. The ion distribution reaches the peak value around 1200 nm in depth. Pure Fe with the displacement energy E_d = 40 eV was adopted for SRIM calculations. The dose and dose rate at a depth of 300 nm were used for damage parameters. The applied dose rate was fixed at 1.74×10^{-3} displacement per atom (dpa)/s at the peak or 0.7×10^{-3} dpa/s at the depth of 300 nm. The dosages reached 3 and 30 dpa, respectively. A 6 mm × 6 mm ion beam was used in order to ensure full coverage of the samples. The detailed parameters are shown in Table 2.

2.2 Sample Preparation for Microstructure Observation

After ion-irradiated, the samples were cut from the sample center along the irradiation direction. The cutting face of the sample was polished and etched with 5 vol.% Nital. The microstructure of the etched samples was examined using the field emission environmental scanning electron microscope (FEE-SEM, Quanta 200F).

Thin foils for TEM observation were cut vertical to the irradiated surface along the ion irradiation direction using the Zeiss Auriga Crossbeam focused ion beam system. The foils were then subjected to low-energy ion sputtering at 150 V using an ultralow-energy Ar ion beam sputtering system to make local area thin enough for electron transmission. Observations were conducted using a field emission transmission electron microscope (FE-TEM, F20). Analysis of radiation-induced defects was carried out at a depth of 300 nm from the surface of the irradiated samples.

2.3 Nano-Indentation Experiments

Due to the small penetration depth of ions, the samples could not be machined into tensile samples or compression samples. Therefore, nano-indentation tests were used to evaluate the mechanical properties of ion-irradiated materials. The nano-indentation hardness at room temperature was measured using a Nano Indenter XP (MTS, USA) with a 2 μm Berkovitch indenter. The maximum load of the equipment is 500 mN. The continuous stiffness measurement (CSM) was carried out to obtain the depth (h) profile of nano-hardness (H) up to a depth of about 2000 nm. Five indentations were made on the irradiated surface of each sample, and the average of the data was adopted.

The tip geometry calibration process is highly important and influential on results. In this process, the molten silicon has been used as the standard sample to calculate the area coefficient. And then, the area function could be expressed as follows (Eq 1) (Ref 19),

$$A_c = f(h_c)$$
$$= \frac{24.44}{h_c} + 101.019 h_c + 4.75 h_c^{\frac{1}{3}} + 1194.42 h_c^{\frac{1}{5}} - 1435.13 h_c^{\frac{1}{7}}$$

(Eq 1)

where A_c is the projected contacted area;

h_c is the contact depth and is defined as the depth of the indenter in contact with the sample under load;

The tip is regularly calibrated with standard samples. The area coefficient is revised based on the deviation result to obtain the appropriate area function.

Although the flux changes with the depth from sample surface which results in variation of the nano-hardness with the depth, the depth of 300 nm was designed as the reference point and for further analysis. Therefore, the I3 and I30 irradiated samples are all talking about the damage of 300 nm in depth under dose rate of 0.7×10^{-3} dpa/s. When the same properties of different doses are discussed, there is no flux effect.

3. Results

3.1 Microstructure

The microstructure of the unirradiated sample (I0 sample) could be found in our earlier studies (Ref 22), which show that Cr-rich $M_{23}C_6$ and Ni-rich M_6C carbides are the main precipitates distributed along grain and/or lath boundaries in the as-received state, the coarse carbides precipitated along grain boundaries are M_3C-type carbides, and the fine M_2C-type carbides are also dispersed inside laths. The microstructure after

Table 1 Chemical composition of SA508-IV RPV steel (wt.%)

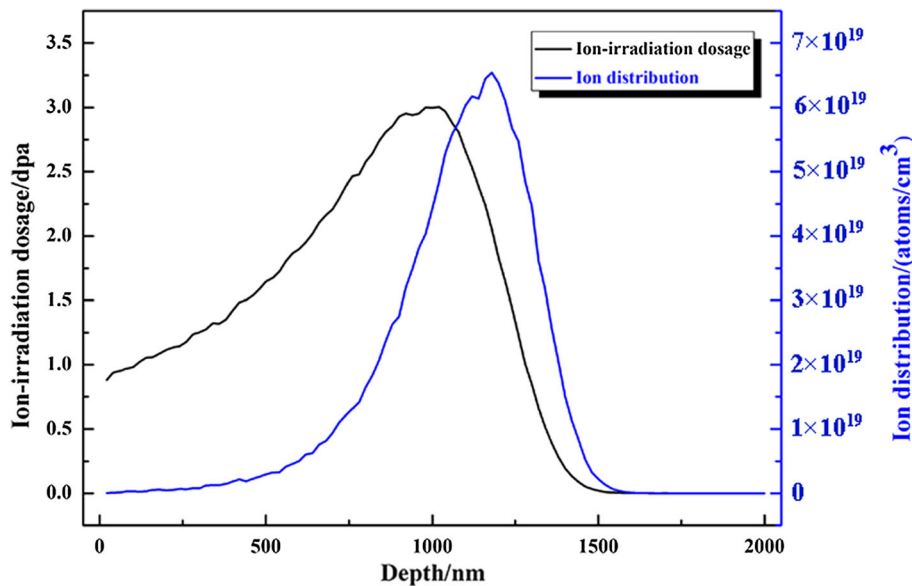| C	Si	Mn	P	S	Ni	Cr	Cu	Mo	Al	Fe
0.15	0.36	0.34	0.011	0.008	3.26	1.66	0.041	0.46	0.005	Balance

Fig. 1 Depth profile of ion-irradiation dosage and ion distribution under 3.5 MeV Fe^{2+} ion irradiation

Table 2 Ion-irradiation parameters

Ion-irradiation dosage, dpa	Fluence, cm^{-2}	Duration, min	Sample no.
0	…	…	I0
3	7.38×10^{15}	42.03	I3
30	7.38×10^{16}	420.3	I30
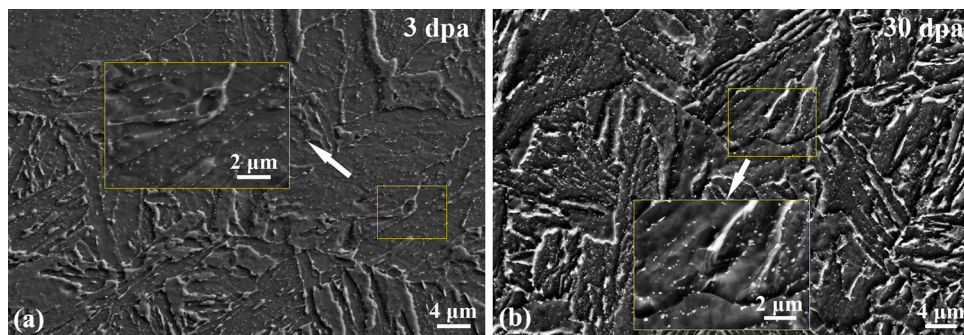
Fig. 2 Microstructure of (a) I3 and (b) I30 ion-irradiated samples under FEE-SEM

irradiation is observed using FEE-SEM and shown in Fig. 2. Fig. 2(a) and (b) represents the microstructure of RPV steel after irradiation for 3 (I3 sample) and 30 dpa (I30 sample), respectively. In order to display the particles clearly, a small area was enlarged in each picture as indicated by the arrows in Fig. 2. It could be noticed that the number of tiny M_2C-type carbides inside laths of I30 sample (Fig. 2b) is more than that of I3 sample (Fig. 2a). The coarse precipitates of $M_{23}C_6$ and M_3C distributed along grain boundaries also show the increasing trend from I3 sample to I 30 sample. The particle size distributions of the irradiated samples have been plotted in Fig. 3. The software image J has been employed to statistically analyze three different view fields of each state. Figure 3(a) is particle size distribution of I3 sample, while Fig. 3(b) shows the particle size distribution of I30 sample. The size of precipitates

in I3 sample has been statistically averaged as 94 nm, and that in I30 sample is around 166 nm, which means the size of precipitates in I30 sample is larger than that in I3 sample. Klueh et al. (Ref 23, 24) demonstrate that the fine M_6C precipitates with high-density form in the high-nickel RPV steels after irradiations. Thus, it could be inferred that the precipitates induced by the irradiation in this high-nickel SA508-IV RPV steel are M_6C carbides.

The STEM mode of FE-TEM is employed to study the elements mapping in order to get the cluster's evolution in the irradiation process. Figure 4, 5, 6 are the microstructure and elements distribution of I0, I3, I30 samples, respectively. In the as-received sample (0 dpa), there are no Cu-rich clusters found (Fig. 4). However, there are obvious CRCs in I3 sample, shown in Fig. 5(a). Thus, CRCs could be considered as the main
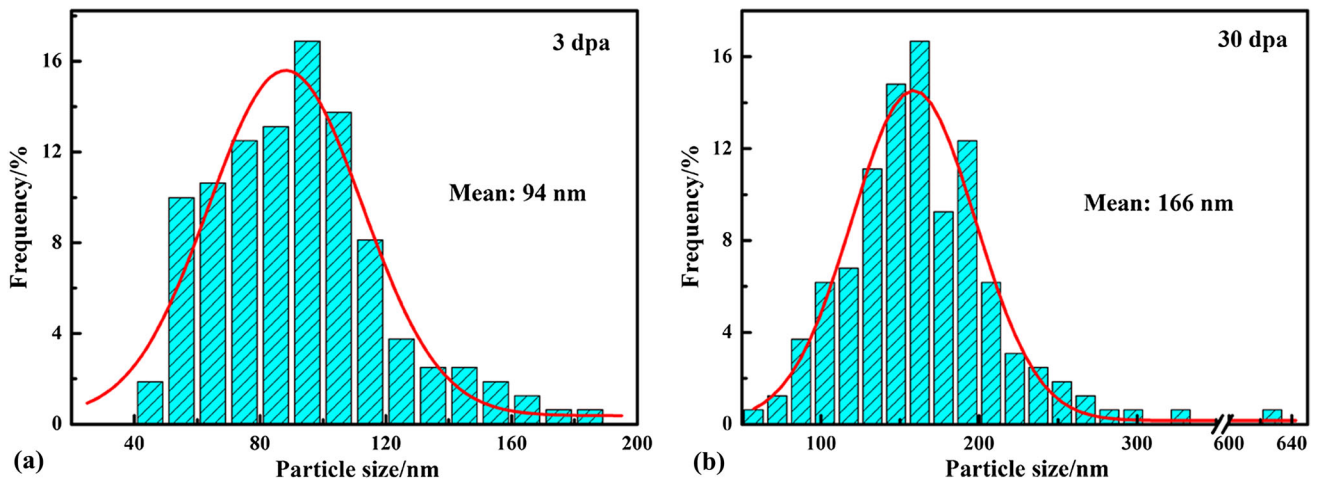
Fig. 3 Particle size distribution of samples with different irradiation dosages: (a) I3 (3 dpa); (b) I30 (30 dpa)
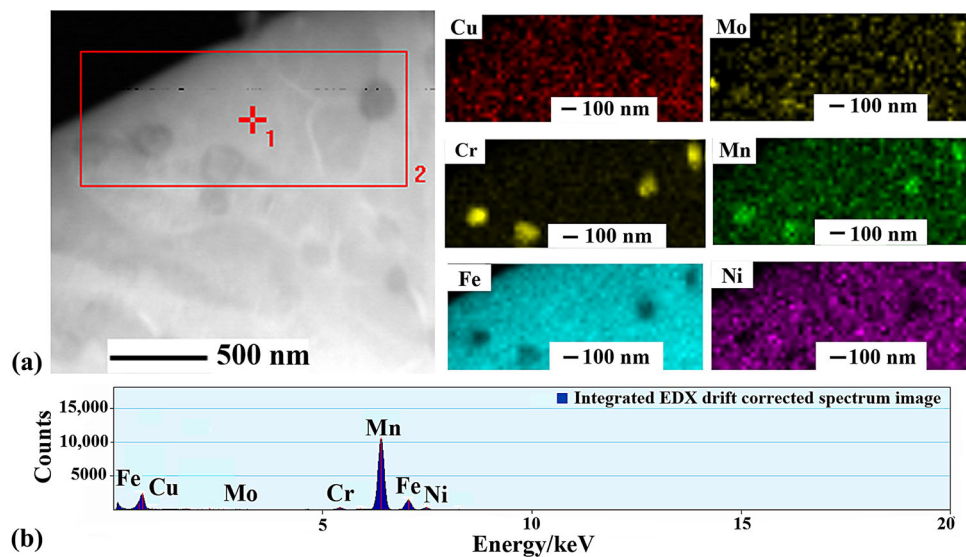

Fig. 4 Microstructure and elements distribution of I0 sample (as-received 0 dpa) under scanning transmission electron microscope (STEM) mode of FE-TEM: (a) STEM image of precipitates and elements mapping measured under STEM; (b) elements intensity in red square area in (a)

irradiation-induced clusters, which play a key role in the microstructure evolution (Ref 15). Cu mapping in Fig. 6(a) of I30 sample shows much less CRCs compared with that of I3 sample, which implies that the number of CRCs decreases with the increase in the irradiation dosage. The volume fraction has been shown in Fig. 7, CRCs in I3 sample account for 9.1‰, whereas those in I30 sample just account for 4.5‰.

It can be seen from Fig. 5 that the precipitates contain mainly Cr with some Mn, whereas Mo seems to distribute inhomogeneously as well. When irradiation dose goes up to 30 dpa, Mo atoms segregate together with Cr and Mn atoms to form Cr/Mn/Mo-rich precipitates, as shown in Fig. 6. It seems that the contents of Mn and Mo elements in the precipitate in Fig. 6 are higher compared to the contents of Mn and Mo shown in Fig. 5, which means that the segregation of Mn and Mo has been enhanced by the ion-irradiation. The reasons could be explained as follows. As the dose goes up to 30 dpa, Cr, Mn and Mo atoms come out as self-interstitial atoms. The increase in the number of interstitials available for cluster will promote the interstitial cluster growth rate. Cr/Mn precipitates

existing in the initial irradiation stage will serve as nucleation sites for Mo atoms to settle down due to a slight positive bias in the flow of self-interstitial atoms. Therefore, Cr/Mn precipitates become larger and Mo atoms also take part in the precipitate formation in the sample with higher irradiation dose (30 dpa) (see Fig. 6). Cr/Mn/Mo-rich phase is expected to form in low Cu and high Ni content steels irradiated to high doses.

In this SA508-IV RPV steel, Cr, and Ni contents are much higher than those in SA508-III steel, whereas Cu and Mn are much lower. This adjustment of composition could reduce the formation of CRCs and Cr/MnMo rich precipitates, thus reducing the irradiation embrittlement tendency. The increase in Cr and decrease of Mn would all lead to the reduction of ductile of the steel. Therefore, the addition of Ni could make up the loss of mechanical properties of SA508-IV steel.

The substructure evolution of SA508-IV steel under ion-irradiation observed by TEM should also be concerned. It could be seen from Fig. 4(a) that the I0 sample shows few dislocations. There could also be found that the dislocations tangle together in I3 sample (Fig. 5a). The dislocation loops are
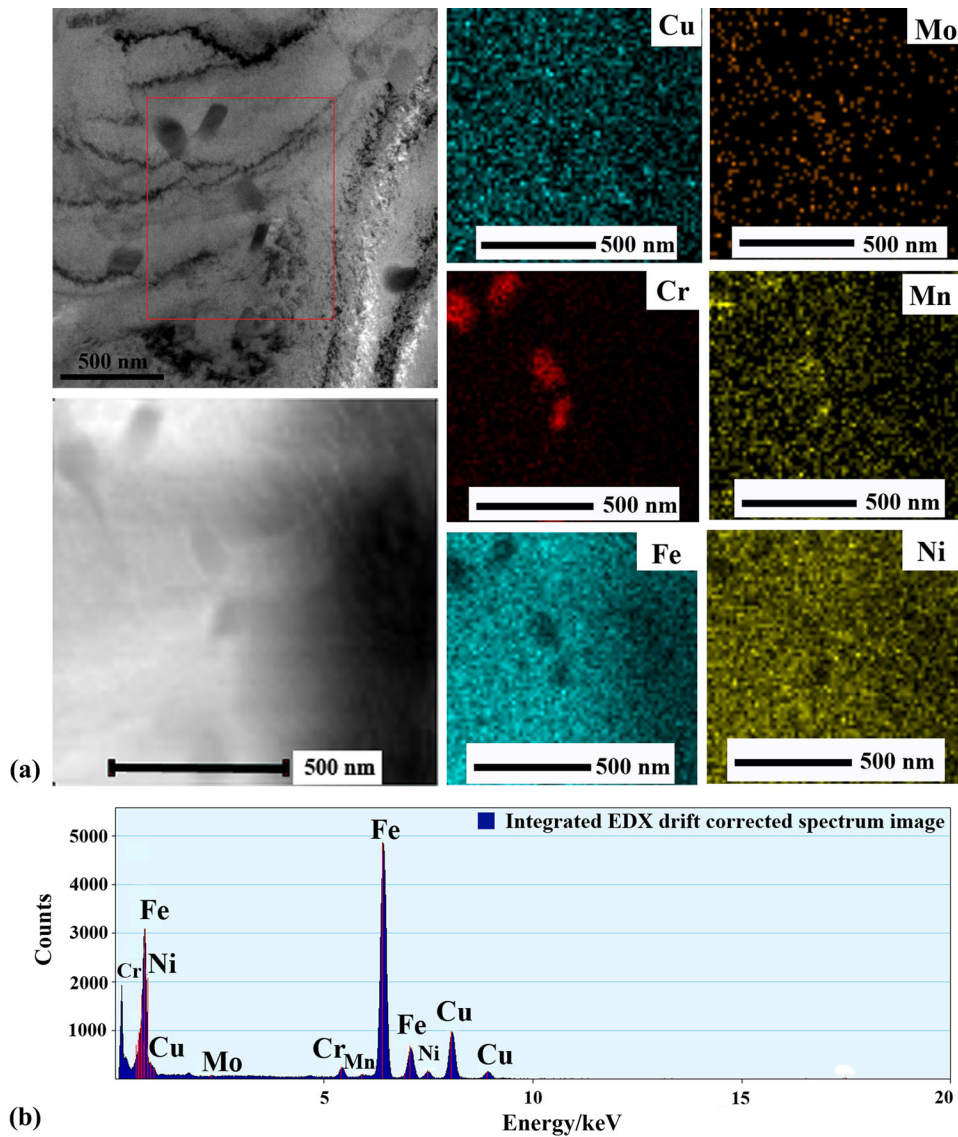
Fig. 5 Microstructure and elements distribution of clusters formed in I3 ion-irradiated sample under STEM mode of FE-TEM: (a) STEM image of clusters and elements mapping measured under STEM; (b) elements intensity in red square area in (a)

formed in I30 sample irradiated after 30 dpa (Fig. 6a) but not in I3 sample. The size of dislocation loops in I30 sample is about 10-20 nm. This indicates that the formation of the loops requires a certain level of interstitial density created by the ion-irradiation or the collapse of the vacancy clusters. Dislocation loops play an important role in irradiation hardening through obstruction to dislocation motion and in other performance of metal and alloys (Ref 7, 9). It has been reported that the dislocation loops caused by ion irradiation are mainly interstitial-type ones (Ref 7, 12). Previous research (Ref 25-27) showed that Ni and Mn elements can promote the formation of the interstitial dislocation loops during irradiation.

3.2 Nano-Indentation Test Results

The ductile-to-brittle transition temperature is usually used to evaluate the mechanical properties (Ref 28). As for the tiny sample could not be fabricated into Charpy impact sample, the microhardness would be employed to judge the mechanical properties (Ref 29). Furthermore, the ion-irradiated layer is too thin for the microhardness test. Therefore, the nano-indentation tests were carried out for I3 and I30 irradiated samples as mechanical tests. The results are shown in Fig. 8. The depth profiles of the nano-hardness of I3 and I30 irradiated samples are plotted in Fig. 8(a) together with results for the I0 (0 dpa) sample, whereas the depth profiles of modulus of the three states are given in Fig. 8(b). From Fig. 8(a), it can be seen that, generally, the nano-hardness of the steel increases with the increase in the irradiation dose, and for each irradiation state, the nano-hardness reaches the highest value, 13.40 GPa (0 dpa), 18.79 GPa (3 dpa), 24.90 GPa (30 dpa), respectively, right at the surface and then decreases with the increase in the measured indentation depth. For I0 sample curve, the nano-hardness sharply drops to about 5 GPa after the highest point. It can be assumed that the maximum peak value of I0 sample represents the original hardened surface condition. The increment of the peak values of I3 sample and I30 sample curves can then be considered as the ion irradiation hardening effect at the surface. The I3 sample curve goes through a semi-plateau stage after the initial sharp drop and then gradually decreases with the
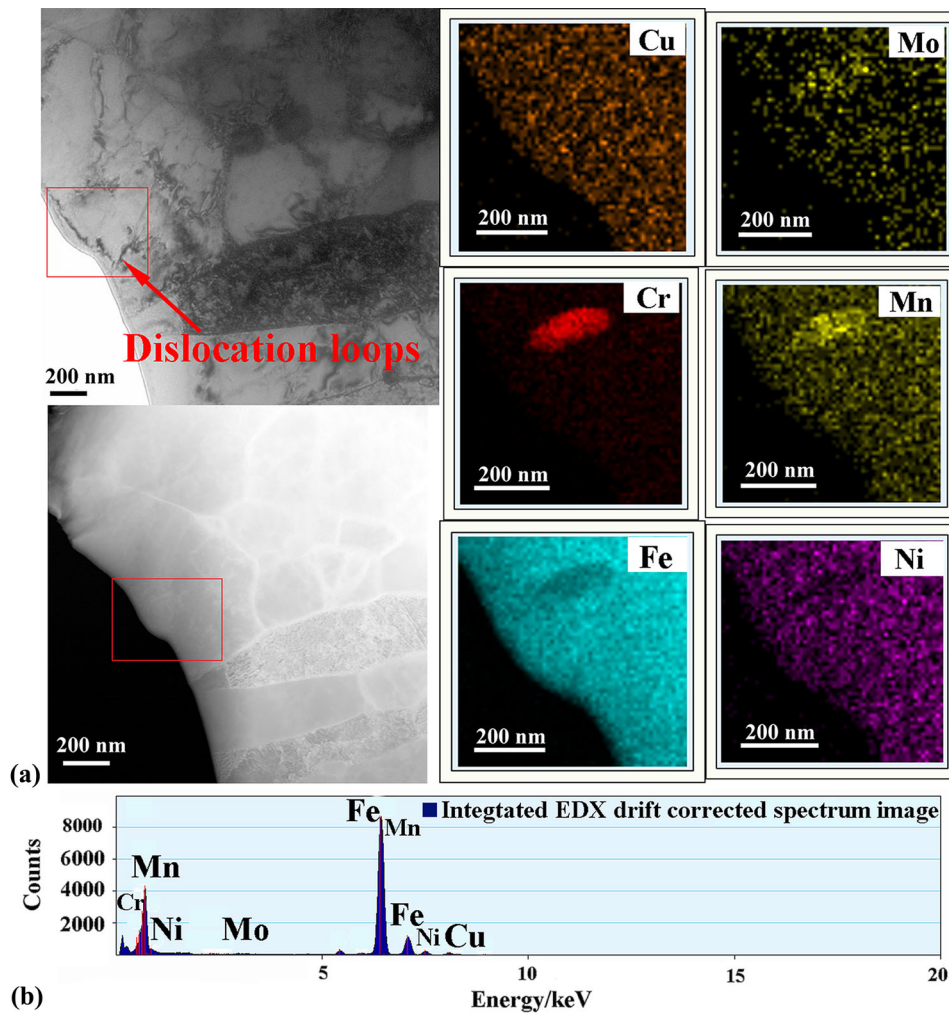
Fig. 6 Microstructure and elements distribution of clusters formed in I30 ion-irradiated sample under STEM mode of FE-TEM: (a) STEM image of clusters and elements mapping measured under STEM; (b) elements intensity in red square area in (a)
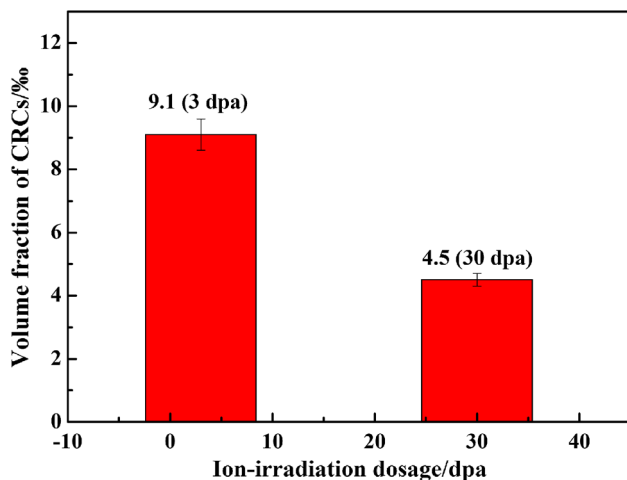

Fig. 7 Volume fraction of CRCs under different ion-irradiation doses

increase in indentation depth to a stable value, while the I30 sample curve goes through a plateau stage after the initial sharp drop and then gradually decreases to the stable stage.

The critical indentation depth corresponding to the constant nano-hardness value for each curve is 1634 nm (2.69 GPa) for I0 sample curve, 1733 nm (3.30 GPa) for I3 sample, and 1781 nm (3.81 GPa) for I30 sample. The difference in the critical depth may be related to the irradiation impact depth corresponding to different doses. The high irradiation dose will produce thick irradiation hardened materials from the surface which will be reflected in the nano-hardness measurement. As the critical indentation depth is unknown before the nano-hardness tests, 300 nm in depth is designated as the reference point for the damage parameters used to calculate the ion irradiation dose and dose rate. The nano-hardness values of the steel samples at indentation depth of 300 nm are 3.89 GPa (0 dpa), 6.88 GPa (3 dpa), 8.45 GPa (30 dpa), respectively, which are much higher than those at the critical indentation depth.

The modulus values of I0, I3, and I30 ion-irradiated samples at around 100 and 300 nm depth are shown in Fig. 8(b). It could be found that the moduli of I0, I3 and I30 samples are 264.7, 293.7, and 300.7 GPa at 100 nm and 249, 254.3, and 256.3 GPa at 300 nm, respectively. The above means the moduli at 100 nm depth increase quickly, whereas the moduli increase a little at 300 nm depth. Therefore, it could be concluded that the moduli reach saturation at around 300 nm depth.
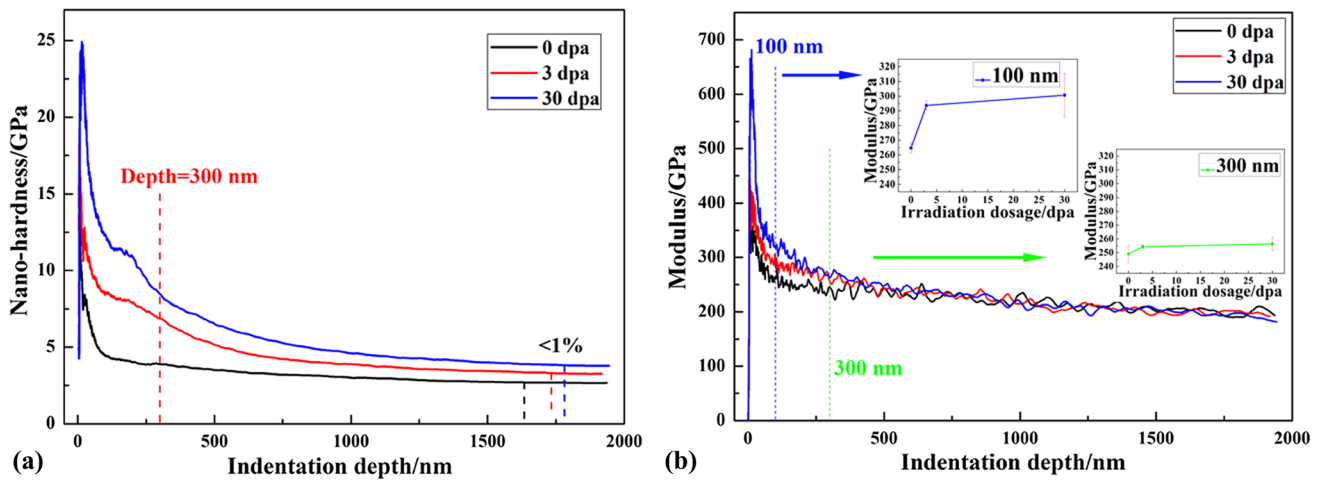
Fig. 8 Depth profiles of nano-hardness (a) and modulus (b) of I0, I3, and I30 ion-irradiated samples

4. Discussion

From the mapping evolution of I0, I3, I30 samples shown in Fig. 4-6, it could be found that the huge irradiation energy enhances the Cr, Mn, Mo atoms comes out as interstitial atoms. The initial segregation would act as nucleation sites for the following precipitates formation and grown-up. Then the particles density and size evolution in Fig. 3 could be explained.

As for the Cu-rich clusters, it has been known that Cu increases the kinetic of clusters formation (Ref 12), thus Cu plays an important part in solute clustering. At the initial stage of ion-irradiation process, the concentration of vacancies increases continuously (Ref 12). Such a high concentration sharply increases the diffusivity of atoms, leading to the enhanced clustering, especially in the case of copper which is highly insoluble in iron at around 290 °C (Ref 30, 31). On the other hand, the displacement cascades cause many point defect clusters, which could be ideal sites for copper clustering when irradiated around 290 °C (Ref 32). Furthermore, the binding energy between Cu and vacancies has been demonstrated very strong in *ab initio* simulations (Ref 33). Based on the above, the concentrated vacancies and the strong bind between Cu and vacancies would result in the constantly increase in CRCs with the dose going up when the irradiation dose is at a relatively lower level. However, after the irradiation dose becomes higher, a huge number of vacancies and self-interstitial atoms will be produced by irradiation. Then, it could be inferred that a large number of vacancies will effectively dilute Cu-Vacancy couplings and reduce the chances of clustering. Therefore, it will become difficult for CRCs to form because too many vacancies want to couple with the very limited number of Cu atoms. This might be the reason why there are less CRCs in I30 sample (Fig. 5a).

The different size distribution of Cu-rich clusters of I0, I3, and I30 sample could be found in Fig. 4-6. Since there are no CRCs in I0 sample, the comparison of I3 and I30 irradiated sample has been summarized in Fig. 9. Figure 9(a) is CRCs distribution observed under STEM and Fig. 9(b) is the corresponding histograms of I3 irradiated sample, whereas Fig. 9(c) is CRCs distribution observed under STEM and Fig. 9(d) is the corresponding histograms of I30 sample. It

could be seen that the size distribution of I30 sample moves in a smaller direction.

It has been stated that Ni has a strong effect on hardening by promoting the formation of CRCs made up of a Ni shell and Cu core (Ref 16, 25). Ni strongly binds with copper and amplifies the effect of copper by increasing the volume of the precipitates (Ref 34). However, the results obtained in this study are totally different. In Fig. 4(a) and 5(a), Cu atoms form clusters but Ni atoms distributed homogenously within the selected area, which means that Ni has no effect on the clustering of copper atoms. It is a surprise because Ni content (3.26%) in SA508-IV RPV steel studied in the present work is much higher than that (0.65%-0.84%) in the alloys discussed in (Ref 26), while Cu contents are quite similar. Logically, Ni should have a stronger effect on CRCs in SA508-IV steel. Further study is necessary to understand the reasons for the difference.

The presence of Mo plays an important role in impeding intergranular P segregation and fracture of steels, which is because of the attractive Mo-P interactions in the grain matrix and a grain-boundary toughing effect of the segregated Mo (Ref 35, 36). As the irradiation dose increases, Mo atoms distribute on the site of Cr/Mn precipitates (Fig. 6). Then, P segregation would occur because of the lack of Mo atoms, resulting in brittle intergranular fracture.

Previous research results (Ref 12, 16, 17, 37) have shown that irradiation can cause the formation of the manganese-nickel rich precipitates (MNPs) in some of the steels. Radiguet et al. (Ref 12) concluded that Cu content and the irradiation time are the crucial influencing factors. In the present study, however, no MNPs were found during STEM observation of the samples ion-irradiated with doses of both 3 dpa (irradiation duration of 42 min) and 30 dpa (irradiation duration of 420 min). This implies that the irradiation time is not decisive in the formation of MNPs. The absence of MNPs in SA508-IV RPV steel is probably because of the high content of Cr (1.66 wt.%). Unlike Ni, Cr is a strong carbide forming element which, together with Mn, could replace Fe atoms to form Cr/Mn carbide precipitates.

It is important to note that the hardness change is expected to be greater for lower dose rate irradiations (1.74×10^{-3} dpa/s at the peak in this study) arising from precipitate of solutes or complex defect structures (Ref 38, 39). The main factors that result in the increase in nano-hardness with the irradiation
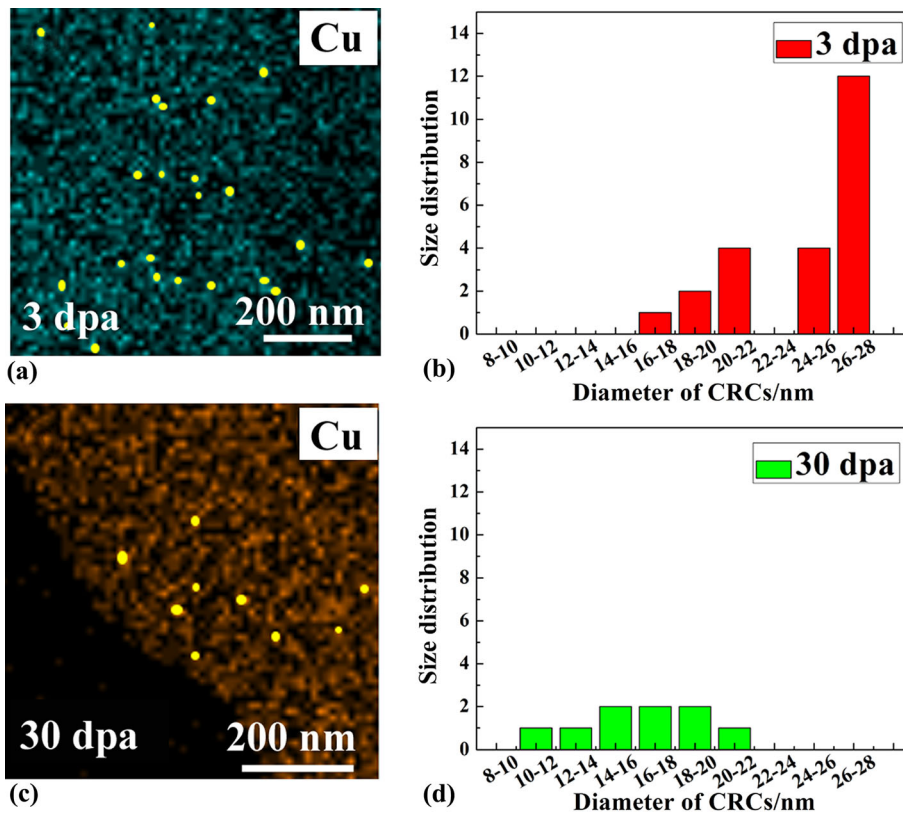
Fig. 9 Different size distributions of CRCs in I3 and I30 samples: (a) CRCs in I3 sample; (b) CRCs size distribution of I3 sample; (c) CRCs in I30 sample; (d) CRCs size distribution of I30 sample

doses are the defects, clusters, and precipitates produced in the ion-irradiation process. It has been demonstrated that the square root of the volume fraction of the solute atom clusters provides a good correlation with the increase in hardness (Ref 14, 40). Besides, as mentioned above, nickel has a strong effect on the formation of the interstitial-type dislocation loops, which will lead to an increase in hardness. When the irradiation dose is higher, the content of Mo in the matrix decreases as a result of the co-segregation with Cr-Mn precipitates (Fig. 5). Mo-P interaction will be reduced, leaving more P atoms free to segregate to the grain boundaries which can result in the hardness increasing.

In Fig. 8(a), the curve of I3 irradiated sample shows a semi-plateau stage and that of I30 sample shows a plateau stage. The mechanism of plateau is usually considered to be due to the saturation of damage. The semi-plateau stage may be corresponding to the saturation of CRCs which form in the initial period of ion-irradiation. However, the plateau in the higher dose I30 sample curve could be attributed to the loop coalescence (Ref 41). From our previous study (Ref 42), it could be known that there is an inflection point on the bilinear curve replotted by nano-hardness curve according to Nix-Gao equation, beyond which the ion-irradiation effect on SA508-IV RPV steel is insignificant.

Modulus is an important parameter that represents the bond strength of the atoms and ions. The variation of the modulus curves could be attributed to the elastic anisotropy of materials (Ref 43). The high-energy ion-irradiation has produced large elastic anisotropy in the materials. Therefore, the I30 irradiated sample possesses highest modulus values. However, the influence of the ion-irradiation just occurs on the top surface.

5. Conclusions

In this study, different doses of ion-irradiation have been employed to study the irradiation sensitivity of this new generation SA508-IV RPV steel. The microstructure of the irradiated samples has been analyzed to study the evolution of the particles under ion irradiation. Then the mechanical properties of different doses samples have been evaluated by nano-indentation experiments in this study. Some main conclusions have been summarized as follows,

(1) Cu-rich clusters formed after ion irradiation by 3 dpa, but partly disappeared when irradiation dose increased to 30 dpa.
(2) Alloying element Mo atoms remained in the matrix after irradiation by 3 dpa. At 30 dpa irradiation, however, Mo segregated to form Cr/Mn/Mo-rich precipitates.
(3) Nano-hardness versus indentation depth curves revealed that samples subjected to ion irradiation by 3 dpa display a semi-plateau stage due to the saturation of Cu-rich clusters; while the I30 sample curve demonstrates a

plateau stage which may be attributed to the loop coalescence.

(4) The ion-irradiation just affects the modulus values of top surface (less than 500 nm) of SA508-IV RPV steel.

Acknowledgments

References

1. T.R. Leax, Temperature Dependence and Variability of Fracture Thoughness in the Transition Regime for A508 Grade 4N Pressure Vessel Steel, *J. ASTM Int.*, 2006, **3**(1), p 1–20.

2. G.L. Wire, W.J. Beggs, T.R. Leax, Evaluation of Irradiation Embrittlement of A508 Gr 4N and Comparison to Other Low-Alloy Steels, Bettis Atomic Power Laboratory (BAPL), West Mifflin, PA, USA, 2002, B-T-3450

3. Y. Zhou, J. Chen, Y. Xu and Z. Liu, Effects of Cr, Ni and Cu on the Corrosion Behavior of Low Carbon Microalloying Steel in a CF-Containing Environment, *J. Mater. Sci. Technol.*, 2013, **29**, p 168–174.

4. Y.T. Chen, D.G. Atteridge and W.W. Gerberich, Plastic Flow of Fe-Binary Alloys-I. A Description at Low Temperatures, *Acta Metall.*, 1981, **29**(6), p 1171–1185.

5. W.W. Gerberich, Y.T. Chen, D.G. Atteridge and T. Johnson, Plastic flow of Fe-binary alloys-II. Application of the description to the ductile-brittle transition, *Acta Metall.*, 1981, **29**(6), p 1187–1201.

6. S. Konovalov, Y. Ivanov, V. Gromov and I. Panchenko, Fatigue-induced Evolution of AISI 310S Steel Microstructure after Electron Beam Treatment, *Materials*, 2020, **13**(20), p 1–13.

7. P.P. Liu, M.Z. Zhao, Y.M. Zhu, J.W. Bai, F.R. Wan and Q. Zhan, Effects of Carbide Precipitate on the Mechanical Properties and Irradiation Behavior of the Low Activation Martensitic Steel, *J. Alloy. Compd.*, 2013, **579**(5), p 599–605.

8. G.S. Was, J.T. Busby, T. Allen, E.A. Kenik, A. Jenssen, S.M. Bruemmer, J. Gan, A.D. Edwards, P.M. Scott and P.L. Andresen, Emulation of Neutron Irradiation Effects With Protons: Validation of Principle, *J. Nucl. Mater.*, 2002, **300**(2–3), p 198–216.

9. G. Gupta, Z. Jiao, A.N. Ham, J.T. Busby and G.S. Was, Microstructural Evolution of Proton Irradiated T91, *J. Nucl. Mater.*, 2006, **351**(1–3), p 162–173.

10. C. Sun, S. Zheng, C.C. Wei, Y. Wu, L. Shao, Y. Yang, K.T. Hartwig, S.A. Maloy, S.J. Zinkle, T.R. Allen, H. Wang and X. Zhang, Superior Radiation-Resistant Nanoengineered Austenitic 304L Stainless Steel for Applications in Extreme Radiation Environments, *Sci. Rep.*, 2015, **5**, p 7801–7807.

11. S.J. Wu and L.W. Cao, Effect of Intergranular Failure on the Critical Fracture Stress and the Fracture Toughness of Degraded Reactor Pressure Vessel Steel, *Int. J. Press. Ves. Pip.*, 2013, **101**, p 23–29.

12. B. Radiguet, P. Pareige and A. Barbu, Irradiation Induced Clustering in Low Copper or Copper Free Ferritic Model Alloys, *Nucl. Instrum. Methods Phys. Res. B*, 2009, **267**(8–9), p 1496–1499.

13. B. Yang, Thermographic Detection of Fatigue Damage of Reactor Pressure Vessel (RPV) Steels, *J. Mater. Eng. Perform.*, 2003, **12**(3), p 345–353.

14. K. Fujii, K. Fukuya and T. Hojo, Concomitant Formation of Different Nature Clusters and Hardening in Reactor Pressure Vessel Steels Irradiated by Heavy Ions, *J. Nucl. Mater.*, 2013, **443**(1–3), p 378–385.

15. F. Hori, A. Morita and R. Oshima, Radiation-Enhanced Precipitation in FeCu(C) Alloys Studied by Electron Microscopy, *J. Electron Microsc.*, 1999, **48**(5), p 585–589.

16. G.R. Odette, Radiation Induced Microstructral Evolution in Reactor Pressure Vessel Steels, *Mat. Res. Soc. Symp. Proc.*, 1995, **373**, p 137–148.

17. G.R. Odette and G.E. Lucas, *Radiat. Eff. Defects Solids*, 1998, **144**, p 189–231.

18. T. Toyama, N. Tsuchiya, Y. Nagai, A. Almazouzi, M. Hatakeyama, M. Hasegawa, T. Ohkubo, E. van Walle and R. Gerard, Irradiation-Induced Changes of the Atomic Distributions around the Interfaces of Carbides in a Nuclear Reactor Pressure Vessel Steel, *J. Nucl. Mater.*, 2010, **405**, p 177–180.

19. X.D. Li and B. Bhushan, A Review of Nanoindentation Continuous Stiffness Measurement Technique and its Applications, *Mater. Charact.*, 2002, **48**, p 11–36.

20. M. Chausov, P. Maruschak, A. Pylypenko and L. Markashova, Enhancing Plasticity of High-Strength Titanium Alloys VT 22 Under Impact-Oscillatory Loading, *Phil. Mag.*, 2017, **97**(6), p 389–399.

21. J.F. Ziegler, J.P. Biersack and U. Littmark, *The Stopping and Range of Ions in Solids*, Pergamon Press, New York, USA, Treatise on Heavy-Ion Science, 1985, p 93–129

22. X. Bai, S.J. Wu and P.K. Liaw, Influence of Thermo-Mechanical Embrittlement Processing on Microstructure and Mechanical Behavior of a Pressure Vessel Steel, *Mater. Des.*, 2016, **89**, p 759–769.

23. R.L. Klueh, N. Hashimoto, M.A. Sokolov, K. Shiba and S. Jitsukawa, Mechanical Properties of Neutron-Irradiated Nickel-Containing Martensitic Steels: I. Experimental Study, *J. Nucl. Mater.*, 2006, **357**(1–3), p 156–168.

24. R.L. Klueh, N. Hashimoto, M.A. Sokalov, P.J. Maziasz, K. Shiba and S. Jitsukawa, Mechanical Properties of Neutron-Irradiated Nickel-Containing Martensitic Steels: II. Review and Analysis of Helium-Effects Studies, *J. Nucl. Mater.*, 2006, **357**(1–3), p 169–182.

25. Y. Nishiyama, K. Onizawa, M. Suzuki, J.W. Anderegg, Y. Nagai, T. Toyama, M. Hasegawa and J. Kameda, Effects of Neutron-Irradiation-Induced Intergranular Phosphorus Segregation and Hardening on Embrittlement in Reactor Pressure Vessel Steels, *Acta Mater.*, 2008, **56**(16), p 4510–4521.

26. H. Shibamoto, K. Kitao, H. Matsui, M. Hasegawa, S. Yamaguchi and A. Kimura, *Effect of Nickel on Irradiation Hardening and Microstructure Evolution of Proton Irradiated Fe-Cu Alloys, Effects of radiation on materials, 20th international symposium, ASTM STP 1405.* S.T. Rosinski, M.L. Grossbeck, T.R. Allen, A.S. Kumar Ed., American Society for Testing and Materials, PA, USA, West Conshohocken, 2001, p 722–733

27. H. Watanabe, S. Arase, T. Yamamoto, P. Wells, T. Onishi and G.R. Odette, Hardening and Microstructural Evolution of A533b Steels Irradiated with Fe Ions and Electrons, *J. Nucl. Mater.*, 2016, **471**, p 243–250.

28. T. Sharma, N.N. Kumar, R. Mondal, K.V.M. Krishna, I. Samajdar and V. Kain, Ductile-to-Brittle Transition in Low-Alloy Steel: A Combined Experimental and Numerical Investigation, *J. Mater. Eng. Perform.*, 2019, **28**(7), p 4275–4288.

29. A. Gandhi, A. Kundu, A. Sarkar, J.K. Mahato and P.C. Chakraborti, Effect of Laser Pulse Duration on Tensile and Electrochemical Behavior of Laser-Welded Dual-Phase Steel, *J. Mater. Eng. Perform.*, 2021, **30**(6), p 4263–4281.

30. M.K. Miller, K.F. Russell, P. Pareige, M.J. Starink and R.C. Thomson, Low Temperature Copper Solubilities in Fe-Cu-Ni, *Mater. Sci. Eng. A*, 1998, **250**(1), p 49–54.

31. G. Salje and M. Feller-Kniepmeir, The Diffusion and Solubility of Copper in Iron, *J. Appl. Phys.*, 1977, **48**(5), p 1833–1839.

32. B. Radiguet, A. Barbu and P. Pareige, Understanding of Copper Precipitation Under Electron or Ion Irradiations in FeCu0.1wt% Ferritic Alloy by Combination of Experiments and Modelling, *J. Nucl. Mater.*, 2007, **360**(2), p 104–117.

33. E. Vincent, C.S. Becquart and C. Domain, Ab Initio Calculations of Self-Interstitial Interaction and Migration with Solute Atoms in bcc Fe, *J. Nucl. Mater.*, 2006, **359**(3), p 227–237.

34. G.R. Odette and G.E. Lucas, Embrittlement of Nuclear Reactor Pressure Vessels, *JOM*, 2001, **53**(7), p 18–22.

35. D.Y. Lee, E.V. Barrera, J.P. Stark and H.L. Marcus, The Influence of Alloying Elements on Impurity Induced Grain Boundary Embrittlement, *Metall. Trans. A*, 1984, **15A**, p 1415–1430.

36. J. Kameda and Y. Nishiyama, Combined Effects of Phosphorus Segregation and Partial Intergranular Fracture on the Ductile-Brittle Transition Temperature in Structural Alloy Steels, *Mater. Sci. Eng. A*, 2011, **528**, p 3705–3713.

37. E. Meslin, B. Radiguet and M. Loyer-Prost, Radiation-Induced Precipitation in a Ferritic Model Alloy: An Experimental and Theoretical Study, *Acta Mater.*, 2013, **61**, p 6246–6254.

38. T. Muroga, H. Watanabe and N. Yoshida, Correlation of Fast Neutron, Fusion Neutron and Electron Irradiations based on the Dislocation Loop Density, *J. Nucl. Mater.*, 1990, **174**, p 282–288.

39. C.D. Hardie, C.A. Williams, S. Xu and S.G. Roberts, Effects of Irradiation Temperature and Dose Rate on the Mechanical Properties of Self-Ion Implanted Fe and Fe-Cr Alloys, *J. Nucl. Mater.*, 2013, **439**, p 33–40.

40. J. Bohmert, H.W. Viehrig and A. Ulbricht, Correlation Between Irradiation-Induced Changes of Microstructural Parameters and Mechanical Properties of RPV Steels, *J. Nucl. Mater.*, 2004, **334**(1), p 71–78.

41. J. Jiang, Y.C. Wu, X.B. Liu, R.S. Wang, Y. Nagai, K. Inoue, Y. Shimizu and T. Toyama, Microstructural Evolution of RPV Steels Under Proton and Ion Irradiation Studied by Positron Annihilation Spectroscopy, *J. Nucl. Mater.*, 2015, **458**, p 326–334.

42. X. Bai, S.J. Wu, P.K. Liaw, L. Shao and J. Gigax, Effect of Heavy Ion Irradiation Dosage on the Hardness of SA508-IV Reactor Pressure Vessel Steel, *Metals*, 2017, **7**(25), p 1–11.

43. P.G. Sanders, J.A. Eastman and J.R. Weertman, Elastic and Tensile Behavior of Nanocrystalline Copper and Palladium, *Acta Mater.*, 1997, **45**(10), p 4019–4025.